RADIAL PARTICLE-IN-CELL SIMULATIONS OF A HALL THRUSTER DISCHARGE WITH DIFFERENT ANOMALOUS TRANSPORT MODELS

17 – 18 – 19 MARCH 2021

A. Marín-Cebrián[(1)], **A. Domínguez-Vázquez**[(1)], **P. Fajardo**[(1)], **E. Ahedo**[(1)]
[(1)]Equipo de Propulsión Espacial y Plasmas, Universidad Carlos III de Madrid, Leganés, Spain,
almarinc@pa.uc3m.es

KEYWORDS: Hall effect thrusters, particle-in-cell simulations, anomalous transport.

ABSTRACT:

Three different anomalous transport models are proposed to account for the empirically-known enhanced cross-field electron transport in a 1D radial PIC model of a Hall effect thruster. Two of them are 'diffusive' models based on an additional 'anomalous' electron collision frequency. The other one is a 'convection' model which adds an effective azimuthal electric field. Collisional models can be isotropic or anisotropic, depending whether anomalous collisions scatter the three velocity components or only those perpendicular to the magnetic field. Four simulations are discussed in this paper, one for each anomalous transport model and one without anomalous effects. For all simulations with anomalous transport, the axial current increases by a factor 10. It is found that the gyroviscous term contribution to the azimuthal electron momentum equation is non-negligible and responsible for the undulating profile of the axial current density. Furthermore, only the collisional models heat the plasma.

1. INTRODUCTION

Hall effect thruster (HET) is one of the most veteran electric propulsion technologies and successfully covers the propulsive needs of a wide range of space missions. Despite the technological maturity of HET, the physics of some relevant phenomena, such as plasma-wall interaction and anomalous transport, are still poorly understood.

Previous works [1–3] have developed a 1D radial (1Dr) kinetic model of a HET discharge, based on the original one by Taccogna [4–6]. This model uses particle-in-cell (PIC) / Monte Carlo Collision (MCC) formulation and takes into account secondary electrons fluxes emitted from the dielectric HET walls. In such low dimensional model there is certain arbitrariness on setting some important plasma parameters. In particular, there is a complex relation between plasma and neutral densities to achieve a self-sustained discharge. To deal with this, the ionization-controlled discharge (ICD) algorithm, presented in Ref. [1], assures a stationary discharge for a prescribed mean plasma density by adjusting the background neutral density. This applies well to the acceleration region of the HET chamber, where plasma-wall recombination and ionization reach an equilibrium. Domínguez-Vázquez et al. [1] observed the depletion of the high energy tails of the electron velocity distribution function (VDF) in the direction perpendicular to the wall. Electrons whose radial velocity is large enough to overcome the Debye sheaths are collected by the walls, explaining the observed electron temperature anisotropy. Furthermore, cylindrical and magnetic mirror effect were found to be non-negligible and responsible for the asymmetries in the plasma discharge. References [1] and [3] provide a comprehensive analysis of the electron radial dynamics focusing on the plasma-wall interaction problem, but lacked a model to account for the empirically-known anomalous cross-field electron transport. Here, anomalous transport is considered and its effects on the electron population are to be investigated.

Experimental measurements reveal an enhanced electron transport not predicted by classical theory. Near wall conductivity (NWC) and azimuthal electron turbulence have been postulated as the two major contributions to this anomalous transport. The latter has been mainly attributed to correlated fluctuations in plasma density and azimuthal electric field, which yield an increase in the axial current. Previous works on the same topic and a 1D modelization [7, 8] have included an anomalous collisionality to deal with the enhanced axial electron transport. This same approach is followed generally by 2D (radial-axial) models of different types (kinetic, fluid, or hybrid) [9–13]. Recent studies have identified three different anomalous contributions in the electron momentum, energy and heat-flux transport equations [14, 15]. Furthermore, most authors model this anomalous collisionality as an isotropic scattering event; while, for others, it only affects the electron velocity components perpendicular to the magnetic field [16–18], thus producing an anisotropic electron scattering. The main goal of this work is to compare different electron turbulence models, assessing their implications on the radial discharge structure.

The article is structured as follows. Section 2. is devoted to summarize the main aspects of the radial kinetic model. Section 3. describes the turbulence

models that have been implemented, discusses on the axial electron current density and analyzes the contributions to the azimuthal momentum balance. Section 4. addresses the effects of the different turbulence models on some relevant plasma magnitudes. Finally, conclusions are drawn on section 5.

2. THE KINETIC MODEL

This section contains a brief description of the 1Dr PIC code. More detailed information can be found in [1]. The radial kinetic model of a given axial cross-section of the HET discharge considers electrons and singly-charged ions (of Xe) as two populations of macroparticles with constant weight W (i.e. number of elementary particles per macroparticle) and time-evolving densities and temperatures, n_j and T_j ($j = i, e$). On the other hand, neutrals are modeled as a spatially homogeneous background with a time-evolving density $n_n(t)$ and a constant temperature T_n. The main model inputs are: (i) the inner and outer radii, r_1 and r_2, (ii) the radially-averaged plasma density $\bar{n}_e$ (constant), (iii) the axial ion velocity u_{zi} (constant), (iv) the axial electric field E_z (constant), (v) the radial magnetic field

$$B_r(r) = B_{r1}\, r_1/r \qquad \text{Eq. 1}$$

and (vi) the SEE characterization of the lateral dielectric walls.

Particle dynamics are driven by (i) collisions among electrons, ions, and neutrals, (ii) the radial magnetic field B_r, (iii) the axial electric field E_z, and (iv) the radial electric field $E_r = -\partial\phi/\partial r$, being ϕ the electric potential. This last one is obtained by solving the 1D radial Poisson equation with appropriate boundary conditions at the dielectric walls. Macroscopic plasma variables are obtained from usual first-order weighting schemes on nodes.

The SEE produced by impacting electrons follows the probabilistic model of [19]. For the simulations to be discussed here only 'true-secondary' electrons will be considered. For low electron impact energies, the SEE yield becomes approximately proportional to the energy of the wall impacting electron. For macroscopic analysis purposes 'secondary electrons' get assigned to the 'primary electron population' after a large angle (>90 deg) Coulomb collision, a collision with neutrals, or an equivalent 'anomalous' process (for those Cases where turbulence is modeled as a collisional event). The collisional, SEE models and the numerical algorithms are described in [1]. For the analyses undertaken here, the set of numerical parameters (cell size, particles per cell, etcetera) are generally those of Tab. 1 of [1]. The reference values of physical parameters for this set of simulations are $r_1 = 35$ mm, $r_2 = 50$ mm, $\bar{n}_e = 4 \cdot 10^{17}$ m^{-3}, $u_{zi} = 10$ km/s, $E_z = 100$ V/cm, and $B_{r1} = 150$ G.

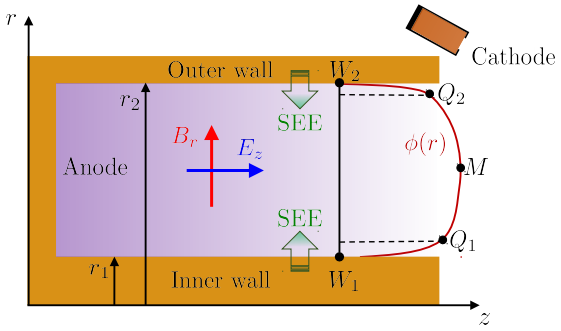

Figure 1: HET radial-axial cross section sketch (adapted from [3]) showing: (i) the imposed axial electric field and radial magnetic field, (ii) secondary emission from the walls, and (iii) the typical potential profile shape. Points M, W_1 and W_2 stand for the mid-radius, inner and outer wall locations respectively. Q_1 and Q_2 represent the approximate location of the sheath edges. The simulation domain corresponds to the thick black line only.

The PIC solution provides the VDFs of ions and electrons. These VDFs, integrated adequately, must satisfy the corresponding fluid (i.e macroscopic equations) for these variables. The macroscopic continuity equation for ions and electrons in 1D cylindrical geometry reads as follows

$$\frac{\partial n_j}{\partial t} + \frac{1}{r}\frac{\partial}{\partial r}(r n_j u_{rj}) = S_{prod}, \quad j = i, e \qquad \text{Eq. 2}$$

where $S_{prod}(\equiv n_e n_n)$ is the plasma volumetric production by electron-bombardment ionization. Steady-state conditions on $n_n(t)$ are sought in order to satisfy

$$I_{wall} \simeq I_{prod}, \qquad \text{Eq. 3}$$

where these two plasma currents (per unit of axial length) are the radially integrated magnitudes of the left and right sides of Eq. 2 representing plasma recombination at the two lateral walls and ionization production respectively. This model considers negligible both the axial or azimuthal injection and depletion of plasma, i.e. there are no axial or azimuthal sources or sinks of particles. For this to be consistent, the numerical algorithms were designed to assure that no secular axial acceleration of ions and electrons exist (at least within the maximum simulation time). Moreover, no particle refreshing is performed and azimuthal or axial derivatives are not considered ($\partial/\partial z = \partial/\partial\theta = 0$).

3. CROSS-FIELD TRANSPORT PHENOMENOLOGICAL MODELS

Electron anomalous cross-field transport effects are analyzed here with three different *ad hoc* models, which use to be justified on azimuthal plasma turbulence. The first one is the anomalous 'isotropic diffusion' model, implemented by [11–13, 20], which defines an anomalous collisionality frequency, ν_{ano},

Type and units	Symbol	Case 0	Case 1	Case 2	Case 3
Anomalous transport model ( )	$E_{\theta,ano}/E_z$	0	0.01	0	0
	ν_{ano}/ω_{ce}	0	0	0.01 (i)	0.01 (a)
Axial electron current (A)	I_{ze}	0.25	2.35	2.26	2.34
Current ratio ( )	$jI_{\theta e}j/I_{ze}$	844.3	89.4	92.5	90.4
Collision frequencies (MHz)	$\bar{\nu}_{ei}$	0.299	0.305	0.091	0.102
	$\bar{\nu}_{en}$	3.771	3.776	1.654	1.394
Neutral density ($10^{17}\ m\ \ ^3$)	n_n	62.5	62.7	25.6	21.4
Electron temperature (eV)	$T_{e,M}$	6.97	6.96	31.17	26.72
SEE yields ( )	$\hbar\delta_{SEE,1}i$	0.16	0.16	0.46	0.26
	$\hbar\delta_{SEE,2}i$	0.30	0.29	0.72	0.83
Current densities (A/m^2)	$jj_{re,1}\ \ j$	82	81	345	133
	$jj_{rs1,1+}j$	13	13	159	34
	$jj_{re,2+}j$	127	127	665	950
	$jj_{rs2,2}\ \ j$	38	37	480	793
Energy balance contributions (W/cm)	P_{E_z}	24.9	235.3	226.1	233.9
	P_{E_r}	7.6	7.6	85.5	31.0
	P_{inel}	9.6	9.6	16.4	12.1
	P_{ano}	0	210.4	0	0
	P_{wall}	7.8	7.8	123.7	193.2

Table 1: Main parameters characterizing the steady-state discharge. For all the simulations $B_{r1} = 150$ *G,* $E_z = 100$ *V/cm,* $I_{zi} = 2.58$ *A and* $\bar{n}_e = 4\ \ 10^{17}$ *m* ^{3}.

to scatter electrons isotropically. It can be said that this anomalous model is equivalent to having a virtually enhanced neutral population. The second one is the anomalous 'anisotropic diffusion' model, proposed by [16–18], which uses also an anomalous collision frequency, ν_{ano}, but only the electron velocity components perpendicular to $\boldsymbol{B}$ are scattered (in this case an isotropic scattering is performed for the velocity components in the $z\ \ \theta$ plane, whereas the radial electron velocity remains unchanged). The third one is an anomalous 'convection' model, where a force $eE_{\theta,ano}$, is applied on each electron. This anomalous electric field can be interpreted as

$$E_{\theta,ano} = \hbar\tilde{n}_e\tilde{E}_\theta i/n_e \qquad \text{Eq. 4}$$

where the numerator of the right side is the time and azimuthally averaged turbulent force (divided by the electron charge, e) coming from correlated fluctuations of density $\tilde{n}_e$ and azimuthal electric field $\tilde{E}_\theta$.
Four simulations Cases are used to assess the implications of the three anomalous transport models on the discharge structure: Case 0 does not include anomalous effects; Case 1 simulates the anomalous convection model with $E_{\theta,ano}$ equal to 1% of E_z, i.e. $E_{\theta,ano} = 1$ V/cm; and Cases 2 and 3 simulate respectively the isotropic and anisotropic anomalous diffusion models with a 1% of the electron gyrofrequency ($\nu_{ano} = 0.01\omega_{ce}$), which is $\bar{\nu}_{ano}$ $2.2\ \ 10^7$ s ^{1}. The rest of simulation conditions are identical for the four Cases.
Tab. 1 offers a comparison among the four Cases in terms of macroscopic magnitudes of interest.

3.1. Electron momentum equation

Axial and azimuthal electron currents can be analyzed from the momentum equation. In steady state, this vector equation can be expressed as

$$\mathbf{0} = \quad r\ \bar{\bar{M}}\quad en_e\boldsymbol{E}\quad en_e\boldsymbol{u}_e\quad \boldsymbol{B}+\boldsymbol{F}_{col}+\boldsymbol{F}_{ano}, \qquad \text{Eq. 5}$$

where $\boldsymbol{F}_{col}\qquad m_e n_e \boldsymbol{u}_e(\nu_{en}+\nu_{ei})$ is the resistive force due to collisions with ions and neutrals and the phenomenological force $\boldsymbol{F}_{ano}$ accounts for the anomalous transport macroscopic resultant. Moreover,

$$\bar{\bar{M}} = m_e \int \boldsymbol{v}_e\boldsymbol{v}_e f_e(\boldsymbol{v}_e)d^3\boldsymbol{v} \qquad \text{Eq. 6}$$

is the (symmetric) momentum flux tensor for electrons, with contributions from the electron momen-

tum convection, $\bar{\bar{U}} = m_e n_e \boldsymbol{u}_e \boldsymbol{u}_e$, and pressure tensor,

$$\bar{\bar{P}} = m_e \int \boldsymbol{c}_e \boldsymbol{c}_e f_e(\boldsymbol{v}) d^3\boldsymbol{v}, \qquad \text{Eq. 7}$$

where $\boldsymbol{v}_e = \boldsymbol{u}_e + \boldsymbol{c}_e$ is the electron velocity, being $\boldsymbol{u}_e$ and $\boldsymbol{c}_e$ the electron fluid and thermal velocities respectively. The 'e' subscript is omitted in the three tensors to lighten the notation.

Analyzing the results of $\bar{\bar{M}}$, $\bar{\bar{U}}$ and $\bar{\bar{P}}$ the following conclusions can be extracted. First, $U_{\theta\theta}$ U_{zz}, U_{rr}, since $u_{\theta e}$ u_{re}, u_{ze}. Second, since the electron flow is subsonic (in the Cases under simulation here), the diagonal components of the pressure tensor, $P_{rr} = n_e T_{re}$ and $P_{\theta\theta}$ ' P_{zz} ' $n_e T_{?e}$, dominate over those of $\bar{\bar{U}}$ and show a mild anisotropy. Fig. 2 plots the non-diagonal components of $\bar{\bar{U}}$ and $\bar{\bar{P}}$, these last ones constituting the gyroviscous tensor. Non-diagonal terms of $\bar{\bar{M}}$ are typically 2-3 orders of magnitude smaller than the diagonal ones. Nevertheless, those affecting the azimuthal momentum equation should be taken into consideration, since individual contributions to that equation are also much smaller than for the axial or radial momentum equations. Interestingly, the gyroviscous components have undulating radial profiles, indicating that they are macroscopic remains of the electron gyromotion and radial bouncing.

In all Cases, the axial momentum equation, clearly dominated by strong electric and magnetic forces, reduces to state that the azimuthal fluid velocity corresponds to the *E* *B* drift,

$$u_{\theta e}(r) \text{ ' } E_z / B_r(r). \qquad \text{Eq. 8}$$

Besides, since the average plasma density is the same in the four Cases, the azimuthal current $I_{\theta e}$, defined as

$$I_{\theta e} = 2\pi e \int_{r_1}^{r_2} n_e u_{\theta e} r dr$$
$$I_{\theta e} \quad e \frac{E_z}{B_{rM}} \bar{n}_e \pi (r_2^2 \quad r_1^2) \qquad \text{Eq. 9}$$

is almost identical in all of them: $I_{\theta e}$ 210 A.

The azimuthal component of the electron momentum equation Eq. 5 yields the axial current density, $j_{ze} =$ $e n_e u_{ze}$, as

$$j_{ze} = \frac{1}{B_r}\Big[(r \quad \bar{\bar{M}})_\theta \quad F_{\theta,col} \quad F_{\theta,ano}\Big], \qquad \text{Eq. 10}$$

where

$$(r \quad \bar{\bar{M}})_\theta \quad \frac{1}{r^2}\frac{\partial}{\partial r}(r^2 P_{r\theta}) \qquad \text{Eq. 11}$$

is the gyroviscous tensor divergence contribution.

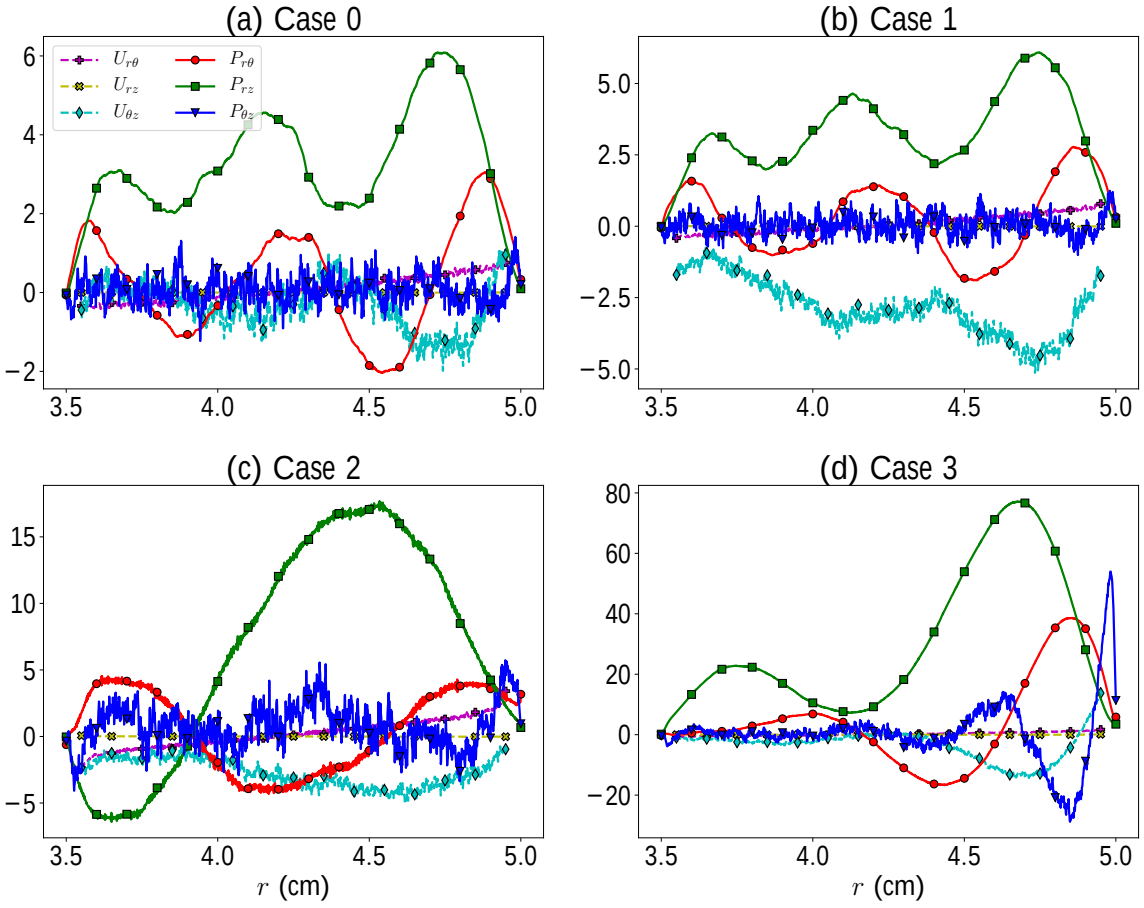

Figure 2: Radial profiles of the non-diagonal components of the electron convection and pressure tensors, $\bar{\bar{U}}$ and $\bar{\bar{P}}$ for Cases 0 to 3 (mPa). Notice the different vertical scales.

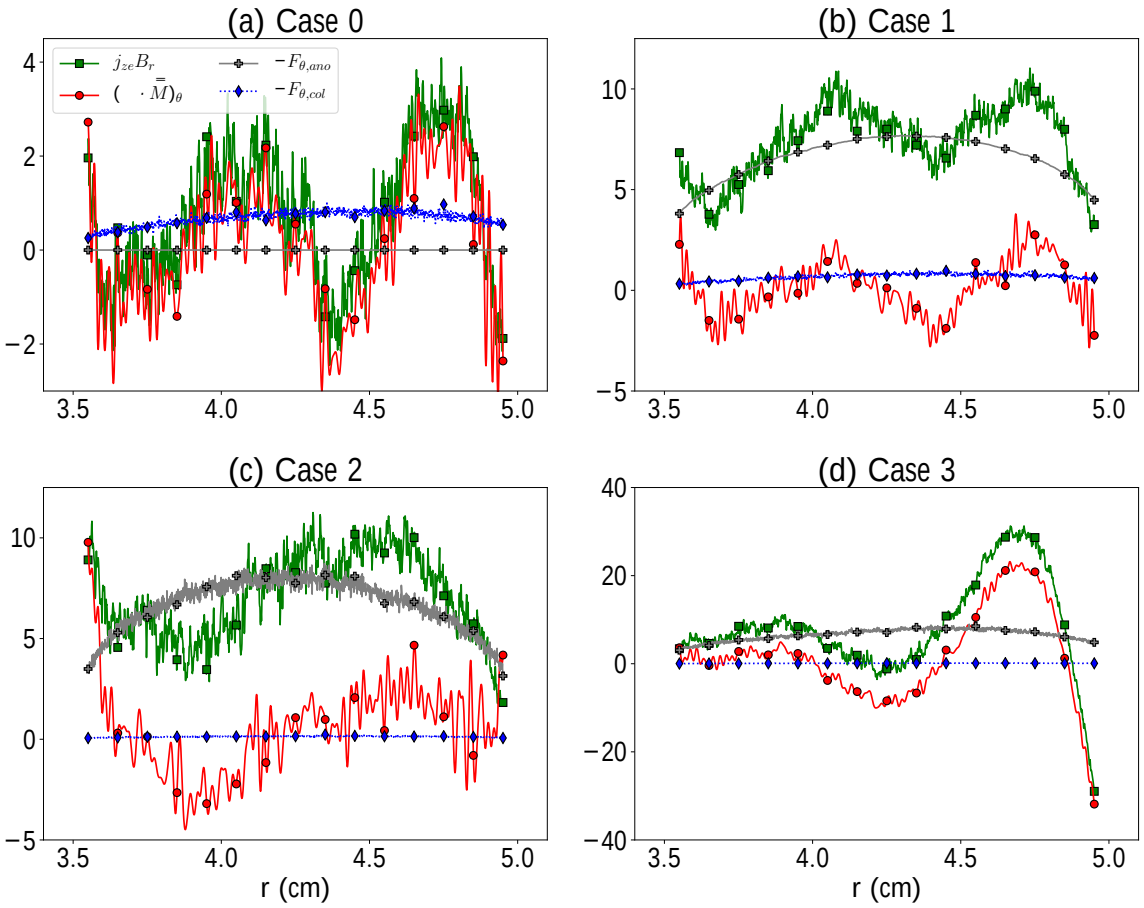

Figure 3: Individual contributions to the azimuthal electron momentum balance of Eq. 10 *for Cases 0 to 3 (N/m^3).*

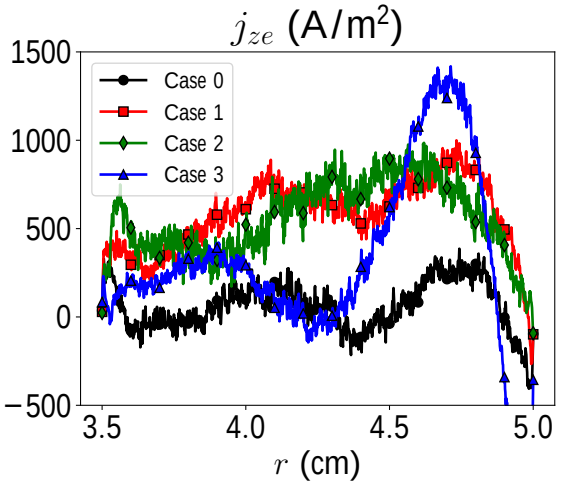

Figure 4: Axial electron current density profiles for Cases 0 to 3 ($j_{ze}/2$ for Case 3)

In the absence of an electric force, three non-dominant order terms compete in balancing the magnetic force. Fig. 3 plots the different forces contributing to Eq. 10. It illustrates well that, in the four Cases, the gyroviscous contribution is important and responsible for the undulating character of $j_{ze}(r)$. Fig. 4 shows that, as expected, j_{ze} is much higher in Cases 1 to 3, which include anomalous transport mechanisms, than in Case 0. The cylindrical asymmetry of $P_{r\theta}$ and $j_{ze}(r)$ is especially evident in Case 3 and it is going to be observed in other variables too.

Integrating Eq. 10 radially, the axial current $I_{ze} = 2\pi \int_{r_1}^{r_2} j_{ze} r dr$ is obtained.

$$I_{ze} \;'\; \frac{2\pi}{B_{r1} r_1} \left(r^2 P_{r\theta}\big|_{r_1}^{r_2} \right. \\ \left. \int_{r_1}^{r_2} r^2 F_{\theta,col}\, dr \quad \int_{r_1}^{r_2} r^2 F_{\theta,ano}\, dr \right). \qquad \text{Eq. 12}$$

Case 0 has I_{ze} ' 0.25 A, very small compared to the empirical evidence (for the parameters used here), since it corresponds to an effective Hall parameter of $jI_{\theta e}j/I_{ze}$ ' 844. Cases 1 to 3 yield very similar axial electron currents, I_{ze} 2.26 2.35 A, ten times higher than in Case 0 and thus $jI_{\theta e}j/I_{ze}$ 90. The contributions of the different forces to the total axial electron current can be obtained from Eq. 12. Due to the undulating radial profile, the net contribution of the gyroviscous term turns out to be rather small for all the Cases: 13%, 1%, 5 % and 9 % for Cases 0 to 3, respectively. Thus, the axial current is driven mainly either by collisionality (as in Case 0 with $F_{\theta,ano} = 0$) or anomalous effects (Cases 1 to 3,

with $F_{\theta,ano}$ $F_{\theta,col}$).
The integration of the kinetic results also shows that the effective azimuthal anomalous force satisfies

$$F_{\theta,ano} = en_eE_{ano,\theta} \quad \text{(convective)} \quad \text{Eq. 13}$$
$$F_{\theta,ano} = m_en_eu_{\theta e}\nu_{ano} \quad \text{(diffusive)} \quad \text{Eq. 14}$$

This implies that, when the anomalous force is dominant (Cases 1 to 3)

$$\frac{I_{\theta e}}{I_{ze}} \quad \frac{E_z}{E_{\theta,ano}} \quad \text{or} \quad \frac{I_{\theta e}}{I_{ze}} \quad \frac{\omega_{ce}}{\nu_{ano}}, \qquad \text{Eq. 15}$$

depending on the anomalous transport model chosen. Cases 1 to 3 present very similar values of I_{ze} just because the right-side values of the last two expressions in Eq. 15 were chosen identical. Since the total electron collision frequency (with the dominance of electron-neutral collisions) is $1.5 \quad 4 \quad 10^6$s ^{1}, anomalous transport dominates for $E_{\theta,ano}/E_z$ or ν_{ano}/ω_{ce} above 0.1-0.2 % provided that $\omega_{ce} \quad 2.2 \quad 10^9$ rad/s.

4. ANALYSIS OF PLASMA PROFILES

Section 3. has shown the effect of different anomalous transport models on the axial electron current density, j_{ze}, and the gyroviscosity tensor. This section analyzes the behavior of other relevant plasma magnitudes.
Tab. 1 shows the neutral density, n_n, required for a self-sustained stationary discharge at a given mean plasma density, $\bar{n}_e = 4 \quad 10^{17}$ m ^{3}. At steady-state the electron production due to ionization must balance the net electron flux to the walls, satisfying Eq. 3. Neutral density decreases with increasing electron temperature, T_e, in order that the resulting ionization rate (which increases exponentially with T_e) assures the same $\bar{n}_e$ in the four Cases. It can be observed that for Cases 0 and 1 n_n is significantly higher than for Cases 2 and 3. Electron-neutral collisions dominate over Coulomb collisions and $e \quad n$ collision frequency is proportional to n_n. Therefore, when neutral density decreases the collision frequency is reduced as a consequence.
The effect of the different anomalous transport models on several plasma magnitudes is plotted in Fig. 5. The parallel (radial) and perpendicular electron temperatures are plotted in Fig. 5 (e) and (f). Cases 0 and 1 have identical T_{re} and $T_{?e}$, while both of them are significantly higher in Cases 2 and 3. This suggests that only the anomalous diffusion models, with their additional electron scattering, heat (anomalously) the plasma. The electron heating mechanisms are analyzed at the end of this section.
In the four Cases the anisotropy ratio $T_{re}/T_{?e}$ is less than one, due to the VDF tails being partially depleted of high energy electrons collected by the wall [1]. Nonetheless, the four Cases present different anisotropy levels: it is $T_{re}/T_{?e} \quad 0.6$ for Cases 0 and 1, 0.8 for Case 2, and $0.2 \quad 0.6$ for Case 3. More unexpected is the large radial asymmetry in $T_{?e}$ for Case 3, which seems to be related to the one in j_{ze} [see Fig 4].
Electric potential profiles, $\phi(r)$ in Fig. 5 (d), present their characteristic shapes with well-distinguished Debye sheaths near the walls. Radial variations of ϕ are proportional to T_{re}, which explains that $\phi(r)$ is identical for Cases 0 and 1 while potential falls are much larger in Cases 2 and 3.
The ion current density $j_{ri}(r)$ is plotted in Fig. 5 (c). Ion (and electron) fluxes come determined by the continuity equation, Eq. 2. Since ionization rate increases with T_e, higher particle fluxes are found in simulations with higher temperatures. Note that the electron fluxes incoming to the wall shown in Tab. 1 are significantly higher than j_{ri} at the wall locations. This is a consequence of the secondary electron emission from the wall. The dielectric condition imposes that the net electron and ion fluxes to the wall must be equal. Since some of the electrons impacting the wall are capable of extracting secondary electrons, effectively reducing the net flux to the wall, a higher number of electrons are required to reach the wall in order to comply with the dielectric condition. Therefore, the wall trades hot electrons coming from the bulk region by cold secondary electrons. The emission of secondary electrons enhances wall loses and contributes to cooling the electron population.
Electron density profiles are plotted in Fig. 5 (a) and all of them share the same mean density, $\bar{n}_e$. The electron density depends mainly on ϕ and the two electron temperatures, through the radial momentum balance [1],

$$T_{re}\frac{\partial \ln n_e}{\partial r} \quad \frac{\partial}{\partial r}(e\phi \quad T_{re}) \; ' \; \frac{1}{r}(T_{?e} \quad T_{re} + m_eu_{\theta e}^2) > 0; \qquad \text{Eq. 16}$$

where collisional and anomalous contributions are negligible. This equation explains why $n_e(r)$ is identical for Cases 0 and 1. The outwards shift of the maximum density increases with the temperature anisotropy, which explain the relative shapes of Cases 1 to 3. In particular the asymmetry of n_e for Case 3 is related to the observed one in $T_{?e}$.
The density of true-secondary electrons, n_s in Fig. 5 (b), is higher in Cases 2 and 3 because electron energies are higher for those Cases; thus leading to higher SEE yields, compiled in Tab. 1. Still, its n_s is at least one order of magnitude smaller than n_e in all the four Cases. Once again, Case 3 exhibits a huge asymmetry in SEE yield ($\hbar\delta_{SEE,1}i = 0.26$ and $\hbar\delta_{SEE,2}i = 0.83$ for the inner and outer wall respectively), which is a consequence of the radial asymmetry of the discharge.
The electron temperature at steady state conditions comes determined by the energy balance,

$$P_{wall} = P_{E_z} + P_{E_r} + P_{inel} + P_{ano}, \qquad \text{Eq. 17}$$

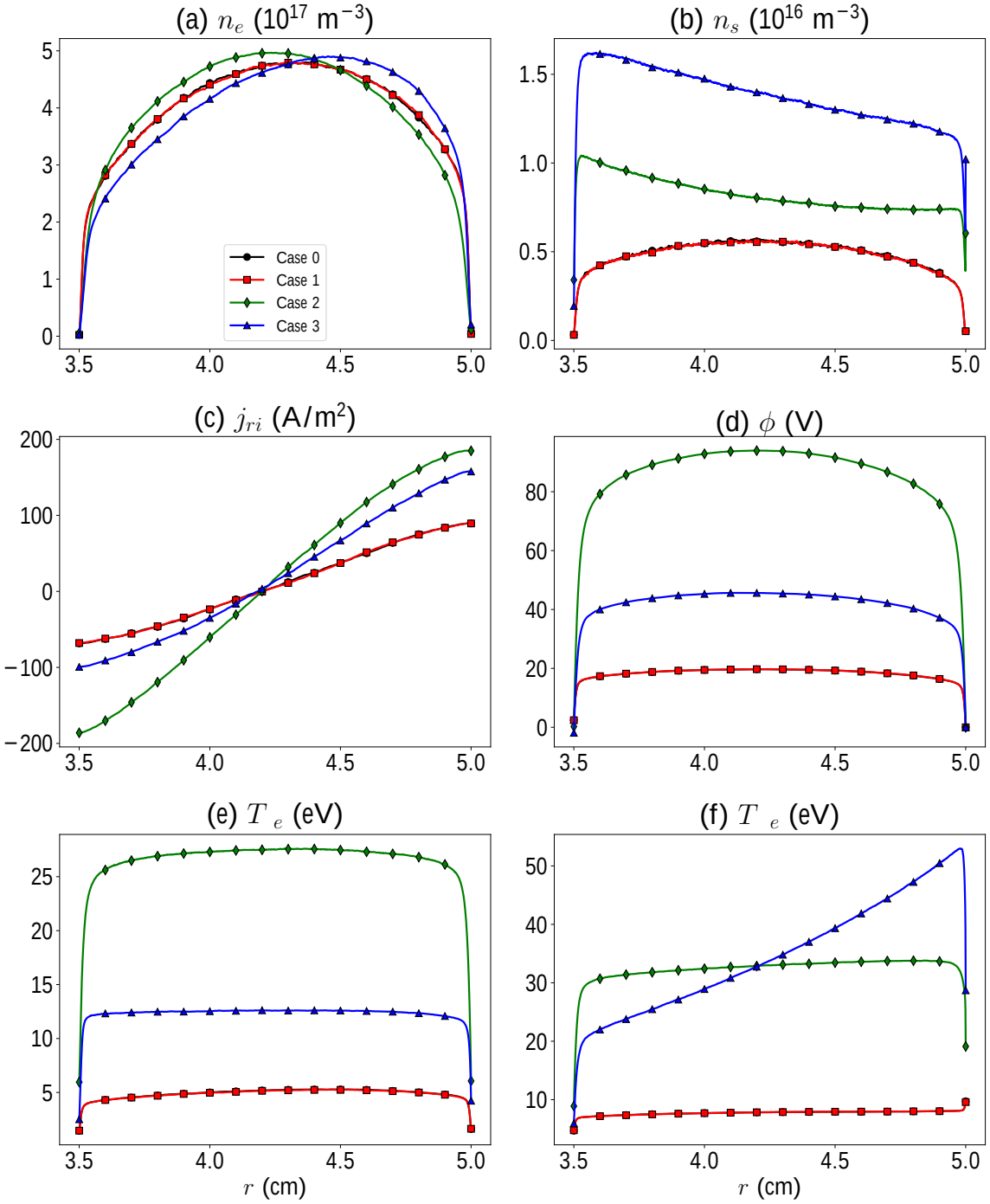

Figure 5: Radial profiles of main plasma magnitudes for Cases 0 to 3.

where P_{wall} is the net power deposited into the walls. P_{inel} stands for the energy spent in inelastic (ionization and excitation) collision processes. P_{E_z} and P_{E_r} are two components of the work done by the electric field on the electron population,

$$P_{E_z} = 2\pi \int_{r_1}^{r_2} j_{ze} E_z r dr = I_{ze} E_z, \qquad \text{Eq. 18}$$

$$P_{E_r} = 2\pi \int_{r_1}^{r_2} j_{re} E_r r dr. \qquad \text{Eq. 19}$$

The work done by the axial electric field acts as a power source ($P_{E_z} > 0$), while the radial electric field contribution is a power sink ($P_{E_r} < 0$); since the electric potential shape opposes to the electron motion toward the walls. Finally, the anomalous contribution to the energy equation can be written in an analogous manner

$$P_{ano} = 2\pi \int_{r_1}^{r_2} \hbar \tilde{j}_{\theta e} \tilde{E}_\theta i r dr \qquad \text{Eq. 20}$$

using the same notation as in Eq. 4. The electron energy balance is complex and non-linear equation, in which all the terms hide a dependence with T_e. The different contributions in Eq. 17 can be found

in Tab. 1. In Case 0, with no anomalous effects, P_{Ez} is small and is spent more or less similarly among the 3 energy sinks (inelastic collisions, negative work of E_r, and walls). In Cases 1 to 3, P_{Ez} is ten times larger as a consequence of having a higher axial electron current. However, this extra energy is spent differently for Cases 1 to 3. In Case 1 the surplus of energy is integrally spent in sustaining the azimuthal plasma turbulence (P_{ano}) and, hence, T_e is the same than in Case 0. In Cases 2 and 3, there is not anomalous contribution to the energy balance ($P_{ano} = 0$) and the surplus of P_{Ez} is absorbed among the other power sinks (primarily to the walls and in second place to P_{E_r}).

5. CONCLUSIONS

In this work three different anomalous transport phenomenological models were implemented in a 1D radial PIC/MCC code [1, 3]. First, a 'convective' model, which assumes that azimuthal turbulence leaves an effective azimuthal electric field acting identically on all electrons, is considered. Then, two 'diffusive' models, which increase the scattering of the electrons and behave as an extra collisional mechanism, were proposed. One of these last models assumes isotropic scattering, and the other one, assumes scattering only in directions perpendicular to the magnetic field.

In order to analyze the effects of these different anomalous transport models on the radial discharge structure, four simulations were run and compared, one for each of the anomalous transport models considered (Cases 1 to 3) and another one with no anomalous effects (Case 0). As expected, Cases 1 to 3 lead to a $(10$ times here) higher axial electron current than for Case 0. Despite the integrated axial current is similar for Cases 1 to 3, radial profiles of the axial current density are very different. The analysis of the azimuthal momentum equation has revealed that the gyroviscous tensor divergence contribution is responsible for the oscillations observed in $j_{ze}(r)$. Although the non-diagonal components of the pressure tensor are typically of 2-3 orders of magnitude smaller than the diagonal terms, they play an important role in the azimuthal momentum balance due to the absence of any other dominant force along that direction.

The 'convective' model does not modify the electron temperature; however, a significant electron heating can be observed in Cases 2 and 3; inducing relevant changes in the discharge structure. At steady state conditions, electron temperature comes determined by the electron energy balance. In Case 1, the additional energy due to the enhanced axial current is completely spent in sustaining the azimuthal plasma turbulence (P_{ano}). For 'diffusive' models $P_{ano} = 0$ and the extra energy is mainly absorbed by the walls.

Three limit Cases to model anomalous transport have been explored in this work. Future work will try to clarify which one (or possible combinations) provides a better representation of real turbulence effects. Further investigations will be carried out to study the local energy balance (here, only the global energy equation was discussed), to analyze radial asymmetries in depth and to determine the role of secondary electrons in the discharge structure. Preliminary studies have shown that the oscillations of $j_{ze}(r)$ are caused mainly by primary electrons, being the role of secondary electrons negligible in cylindrical simulations. Additionally, quasi-planar simulations show that the radial profiles of macroscopic plasma magnitudes become symmetric (as expected) and the oscillations in j_{ze} attenuate in such scenario.

6. ACKNOWLEDGMENTS

The work of Marín and Ahedo has been supported by the PROMETEO-CM project, Grant number Y2018/NMT-4750 (Comunidad de Madrid/FEDER/FSE). Dominguez and Fajardo were supported by Project PID2019-108034RB-I00/AEI/10.13039/501100011033 (Spain's National Research and Development Plan).

7. REFERENCES

[1] Domínguez-Vázquez, A., Taccogna, F., and Ahedo, E., "Particle modeling of radial electron dynamics in a controlled discharge on a Hall thruster," *Plasma Sources Science and Technology*, Vol. 27, No. 6, 2018, pp. 064006.

[2] Domínguez-Vázquez, A., Taccogna, F., Fajardo, P., and Ahedo, E., "Influence of relevant parameters on the radial PIC simulation of a Hall effect thruster discharge," *Space Propulsion Conference*, paper SP2018-288, 3AF, https://www.3af.fr/, Seville, Spain, May 14-18, 2018.

[3] Domínguez-Vázquez, A., Taccogna, F., Ahedo, E., and Fajardo, P., "Parametric study of the radial plasma-wall interaction in a Hall thruster," *Journal of Physics D: Applied Physics*, Vol. 52, No. 47, 2019, pp. 474003.

[4] Taccogna, F., Longo, S., Capitelli, M., and Schneider, R., "Particle-in-Cell Simulation of Stationary Plasma Thruster," *Contributions to Plasma Physics*, Vol. 47, No. 8-9, 2007, pp. 635–656.

[5] F. Taccogna, S. Longo, M. C. and Schneider, R., "Surface-driven asymmetry and instability in the acceleration region of a Hall thruster," *Contrib. Plasma Phys.*, Vol. 48, No. 4, 2008, pp. 1–12.

[6] Taccogna, F., Schneider, R., Longo, S., and Capitelli, M., "Kinetic simulations of a plasma thruster," *Plasma Sources Sci. Technol.*, Vol. 17, No. 2, 2008, pp. 024003.

[7] Ahedo, E., Martínez-Cerezo, P., and Martínez-Sánchez, M., "One-dimensional model of the plasma flow in a Hall thruster," *Physics of Plasmas*, Vol. 8, No. 6, 2001, pp. 3058–3068.

[8] Ahedo, E., Gallardo, J. M., and Parra, F. I., "Analysis of the Plasma Response in a Hall Thruster," Tech. rep., Universidad Politécnica de Madrid. Escuela Técnica Superior de Ingenieros Aeronáuticos., 2002.

[9] Hagelaar, G., Bareilles, J., Garrigues, L., and Boeuf, J.-P., "Role of anomalous electron transport in a stationary plasma thruster simulation," *Journal of Applied Physics*, Vol. 93, No. 1, 2003, pp. 67–75.

[10] Katz, I., Mikellides, I. G., Jorns, B. A., and Ortega, A. L., "Hall2De simulations with an anomalous transport model based on the electron cyclotron drift instability," *IEPC paper*, Vol. 402, 2015.

[11] Szabo, J., Warner, N., Marínez-Sánchez, M., and Batishchev, O., "Full particle-in-cell simulation methodology for axisymmetric Hall Effect Thrusters," *J. Propul. Power*, Vol. 30, No. 1, 2014, pp. 197–208.

[12] Cho, S., Watanabe, H., Kubota, K., Iihara, S., Fuchigami, K., Uematsu, K., and Funaki, I., "Study of electron transport in a Hall thruster by axial–radial fully kinetic particle simulation," *Physics of Plasmas*, Vol. 22, No. 10, 2015, pp. 103523.

[13] Dong, M., Demai, Z., Lei, W., Yongjie, D., Liqiu, W., Hong, L., and Daren, Y., "Numerical simulation study on the influence of channel geometry on discharge characteristics of low-power magnetically shielded Hall thrusters," *Vacuum*, 2020, pp. 109547.

[14] Domínguez-Vázquez, A., *Axisymmetric simulaton codes for Hall effect thrusters and plasma plumes*, Ph.D. thesis, Universidad Carlos III de Madrid, Leganés, Spain, 2019.

[15] Domínguez-Vázquez, A., Zhou, J., Fajardo, P., and Ahedo, E., "Analysis of the plasma discharge in a Hall thruster via a hybrid 2D code," *36th International Electric Propulsion Conference*, paper IEPC-2019-579, Electric Rocket Propulsion Society, https://erps.spacegrant.org, Vienna, Austria, September 15-20, 2019.

[16] Smirnov, A., Raitses, Y., and Fisch, N. J., "Electron cross-field transport in a low power cylindrical Hall thruster," *Physics of Plasmas*, Vol. 11, No. 11, 2004, pp. 4922–4933.

[17] Sydorenko, D., Smolyakov, A., Kaganovich, I., and Raitses, Y., "Kinetic simulation of secondary electron emission effects in Hall thrusters," *Physics of Plasmas*, Vol. 13, No. 1, 2006, pp. 014501.

[18] Kaganovich, I. D., Raitses, Y., Sydorenko, D., and Smolyakov, A., "Kinetic effects in a Hall thruster discharge," *Physics of Plasmas*, Vol. 14, No. 5, 2007, pp. 057104.

[19] Furman, M. A. and Pivi, M. T. F., "Probabilistic model for the simulation of secondary electron emission," *Phys. Rev ST Accel. Beams*, Vol. 5, No. 12, 2002, pp. 124404.

[20] Szabo, Jr., J. J., *Fully kinetic numerical modeling of a plasma thruster*, Ph.D. thesis, Aeronautics and Astronautics Dept., Massachuchusetts Institute of Technology, Boston, February 2001.